Batteries & Supercaps

Research Article
doi.org/10.1002/batt.202500360

Chemistry Europe
European Chemical Societies Publishing

www.batteries-supercaps.org

Structure–Performance Relationships in Anthraquinone-Disulfonate Coordination Polymers for Li-Ion and Na-Ion Battery Cathodes

Catarina Ribeiro, Robert Markowski, Ricardo F. Mendes,* Alberto Fernández-Alarcón, Joaquín Calbo, João Rocha, Alexandru Vlad, and Manuel Souto*

Coordination polymers (CPs) based on organic redox-active moieties offer a promising route to sustainable electrode materials for next-generation batteries. Herein, the synthesis, crystal structure determination, theoretical characterization, and electrochemical evaluation of a series of anthraquinone-disulfonate (AQDS) CPs incorporating Na^+, Mg^{2+}, and Cu^{2+} ions (**AQDS-Na**, **AQDS-Mg**, **AQDS-Cu**) as cathode materials for lithium-ion and sodium-ion storage are reported. Single-crystal X-ray diffraction reveals that **AQDS-Na** adopts a 3D framework, while **AQDS-Mg** and **AQDS-Cu** form 2D layered structures with coordinated water molecules. These structural differences significantly influence the electrochemical performance. For Li-ion storage, **AQDS-Na** delivers an initial capacity of 120 mAh g^{-1}, while **AQDS-Mg** and **AQDS-Cu** show lower initial capacities (95 mAh g^{-1} and 106 mAh g^{-1}, respectively) and faster fading. For Na-ion storage, the performance divergence is even more pronounced: **AQDS-Na** achieves a stable capacity of 91 mAh g^{-1} after 100 cycles, while **AQDS-Mg** and **AQDS-Cu** suffer from significant capacity loss (47 and 18 mAh g^{-1} after 100 cycles, respectively), attributed to the presence of coordinated water molecules in the 2D frameworks. This study highlights the importance of structural dimensionality and coordination environment in designing high-performance cathode materials for battery systems.

1. Introduction

Energy storage devices based on earth-abundant and environmentally friendly elements with high energy density are essential for storing electricity generated from renewable sources.[1] Although lithium-ion batteries (LIBs) are currently the most widely used technology, the high cost of lithium extraction and concerns over limited resource availability could pose significant challenges in the near future. As a result, more abundant and cost-effective elements such as Na^+, Mg^{2+}, and Ca^{2+} are being actively explored for battery applications. In this context, sodium-ion batteries (SIBs) have emerged as a particularly promising alternative due to the low cost and natural abundance of sodium.[2] Furthermore, there is a growing need to replace conventional cathodes based on transition metal oxides to reduce dependence on critical raw materials such as cobalt.[3] Organic electrode materials (OEMs), composed of earth-abundant elements such as carbon, hydrogen, oxygen, and nitrogen, offer a viable alternative thanks to their tunable electrochemical properties and resource sustainability.[4–9] However, a major challenge for OEMs is their solubility in conventional battery electrolytes, often leading to fast capacity fading. Several strategies have been proposed to address this issue, including electrolyte optimization,[10] formation of organic salts,[11,12] incorporation of strong supramolecular interactions,[13,14] and polymer-based approaches.[15,16] The latter encompasses the development of

C. Ribeiro, J. Rocha, M. Souto
Department of Chemistry, CICECO-Aveiro Institute of Materials
University of Aveiro
3810-393 Aveiro, Portugal
E-mail: manuel.souto.salom@usc.es

R. Markowski, A. Vlad
Institute of Condensed Matter and Nanosciences
Molecular Chemistry
Materials and Catalysis
Université Catholique de Louvain
Louvain-la-Neuve B 1348, Belgium

R. F. Mendes, M. Souto
CiQUS
Centro Singular de Investigación en Química Bioloxica e Materiais Moleculares, Departamento de Química-Física
Universidade de Santiago de Compostela
15782 Santiago de Compostela, Spain
E-mail: ricardo.faria@usc.es

A. Fernández-Alarcón, J. Calbo
Instituto de Ciencia Molecular (ICMol)
Universidad de Valencia
46980 Paterna, Spain

M. Souto
Oportunius
Galician Innovation Agency (GAIN)
15702 Santiago de Compostela, Spain

Supporting information for this article is available on the WWW under https://doi.org/10.1002/batt.202500360

conventional redox polymers,[15,17] covalent organic frameworks (COFs),[18–20] coordination polymers (CPs) and metal-organic frameworks (MOFs).[21,22] Understanding how the structure of these materials correlates with their electrochemical performance is crucial for the rational design of next-generation electrodes.

Anthraquinone (AQ), a redox-active organic molecule with high theoretical capacity and excellent electrochemical stability, has been widely studied as an OEM for various rechargeable battery systems.[23,24] To prevent dissolution, AQ moieties have been incorporated into polymers,[25–27] COFs,[28–31] and MOFs,[32–34] enabling their application as stable cathode materials. Additionally, introducing functional groups such as phosphonates[35–37] and sulfonates[38–40] into the framework has shown promise for enhancing energy storage performance. In particular, sodium 9,10-anthraquinone-2,6-disulfonate (AQDS) has been explored as an organic salt cathode material for Li-ion[41] and Na-ion storage,[42] showing good cycling stability in both systems. While AQDS-based MOFs have been previously investigated for photoanode and catalytic applications,[43–45] their potential in energy storage remains largely unexplored.

Here, we report the synthesis and characterization of a series of **AQDS CPs** (**AQDS-Na**, **AQDS-Mg,** and **AQDS-Cu**) incorporating different metal ions (Na^+, Mg^{2+}, Cu^{2+}), evaluated as cathode materials for Li-ion and Na-ion storage. Although the three **AQDS CPs** show similar theoretical specific capacities, they exhibit important structural differences that strongly influence their electrochemical behavior. Specifically, **AQDS-Mg** and **AQDS-Cu** deliver lower practical capacities than **AQDS-Na** when deployed as cathodes for sodium-ion storage. Crystallographic analysis reveals that **AQDS-Mg** and **AQDS-Cu** adopt 2D layered structures incorporating coordinated water molecules, a feature that significantly influences their electrochemical performance. In addition, quantum-chemical calculations indicate relevant charge transport pathways along the AQDS stacking, but the large bandgap, dominated by the organic ligand, precludes good intrinsic electronic conductivity. Such structure–performance correlations are crucial for guiding the molecular design of redox-active CPs optimized for high-performance cathodes for LIB and SIB applications.

2. Results and Discussion

2.1. Synthesis of AQDS CPs

A series of **AQDS CPs** were synthesized to investigate their crystal structures and to correlate structural differences with their electrochemical performance. Commercially available **AQDS-Na** was included in the study, and its crystal structure was determined by single-crystal X-ray diffraction (see below). In contrast, **AQDS-Mg** and **AQDS-Cu** were synthesized from **AQDS-Na** via solvothermal and microwave-assisted methods, respectively (**Scheme 1**a and SI). Specifically, **AQDS-Mg** was prepared by reacting **AQDS-Na** with magnesium acetate tetrahydrate in a water/1-butanol (1:1) mixture at 170 °C for 72 h.[44] **AQDS-Cu** was obtained by reacting **AQDS-Na** and copper nitrate hemi(pentahydrate) under microwave irradiation at 120 °C for 45 min (50 W). The obtained **AQDS CP** crystals were thoroughly washed to remove any unreacted precursors, and their crystal structures were elucidated by single-crystal X-ray diffraction (see below). All three **AQDS CPs** are redox-active: each AQ moiety can undergo reversible reduction to form radical anion and dianion species, which can interact with metal ions such as Li^+ and Na^+ (Scheme 1b).

2.2. Crystal Structure and Physicochemical Characterization of AQDS CPs

All **AQDS CPs** crystallize in the triclinic *P*-1 space group (Table S1, Supporting Information; detailed crystallographic data are provided in the Supporting Information).[46] A comparison of the empirical formulae—Na_2(AQDS)], [Mg(AQDS)$(H_2O)_2$], and [Cu(AQDS)$(H_2O)_2$]—indicates that the degree of protonation and the ligand-to-metal coordination modes are largely consistent across the series. In **AQDS-Na**, the $AQDS^{2-}$ linker coordinates to eight metal centers through various coordination modes. This high degree of connectivity results in a compact 3D structure (**Figure 1**a). The metal centers are arranged in an inorganic layer that propagates along the *b*-axis (Figure S1, Supporting Information), while the $AQDS^{2-}$ linkers stack in a brick-layer arrangement along the *a*-axis. The crystal structure of **AQDS-Mg**

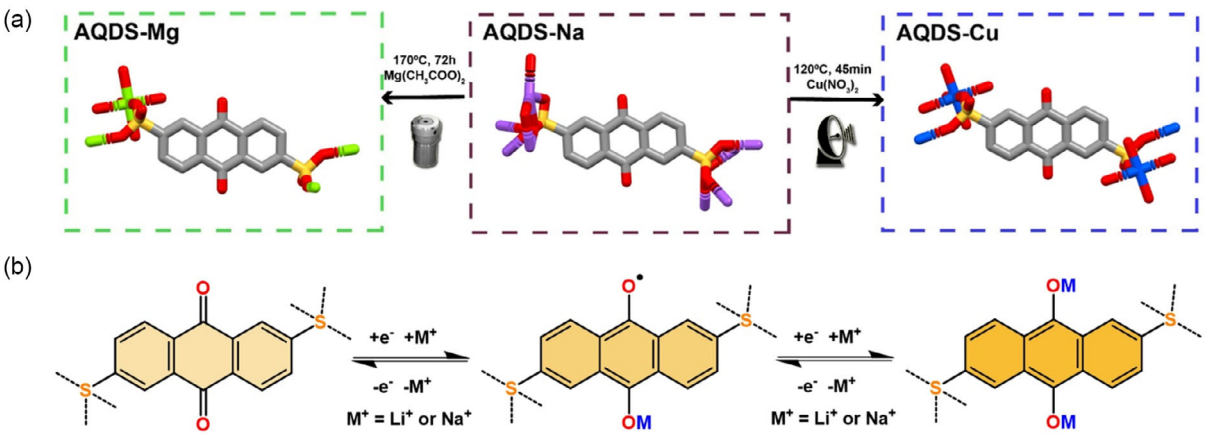

Scheme 1. a) Schematic representation of the synthesis of AQDS CPs. Color code: C (gray), O (red), S (yellow), Mg (green), Na (purple), and Cu (blue). b) Electrochemical mechanism of the redox-active AQDS moieties.

Research Article
doi.org/10.1002/batt.202500360
Chemistry Europe
European Chemical Societies Publishing

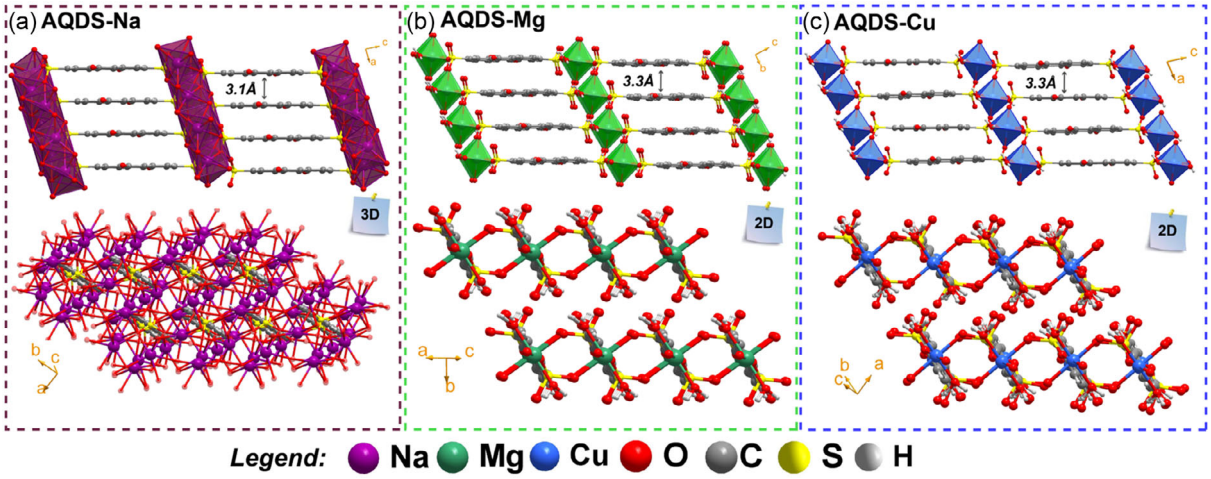

Figure 1. Crystal packing and side views of a) **AQDS-Na**, b) **AQDS-Mg,** and c) **AQDS-Cu,** highlighting the interplanar distances between AQ units and the structural dimensionality: 3D framework for **AQDS-Na** and 2D-layered structures for **AQDS-Mg** and **AQDS-Cu**.

has been previously reported.[44] In this structure, each Mg^{2+} ion adopts an octahedral coordination environment, binding to four symmetry-related $AQDS^{2-}$ linkers and two coordinated water molecules. The presence of coordinated water molecules in **AQDS-Mg** leads to a distinct packing arrangement compared to **AQDS-Na** (Figure 1b). In **AQDS-Mg**, the metal centers form linear inorganic chains, which are connected by the $AQDS^{2-}$ linkers along the *c*-axis, resulting in a 2D-layered structure (Figure S1, Supporting Information). The $AQDS^{2-}$ linkers adopt a brick-layer stacking along the *b*-axis, and the coordinated water molecules inhibit interlayer bonding. Similarly, the crystal packing of **AQDS-Cu** closely resembles that of **AQDS-Mg**: the metal centers are organized into linear inorganic chains, and the two structures are nearly superimposable (Figure S2, Supporting Information). As in **AQDS-Mg**, the metal centers are connected by $AQDS^{2-}$ linkers to form a 2D-layered structure (Figure 1c). Overall, the main structural difference among the three **AQDS CPs** lies in their dimensionality: **AQDS-Na** forms a 3D network, whereas **AQDS-Mg** and **AQDS-Cu** crystallize into 2D-layered structures, with coordinated water molecules present in the latter two. Despite these differences, all materials exhibit a similar brick-layer stacking of $AQDS^{2-}$ linkers, with interplanar distances ranging from 3.1 to 3.3 Å (Figure 1). The phase purity of the **AQDS CPs** was confirmed by powder X-ray diffraction, with experimental patterns matching the simulated ones (Figure S3–S5, Supporting Information).

The physicochemical properties of the **AQDS-CPs** were further investigated through complementary characterization techniques. Fourier transformed infrared (FTIR) spectroscopy of **AQDS-Mg** and **AQDS-Cu** (Figure S6, Supporting Information) revealed broad IR bands between 4000 and 3000 cm^{-1}, corresponding to the υ(*O*-H) stretching modes, consistent with the presence of coordinated water molecules. Thermogravimetric analysis (TGA) further supported this observation, showing a distinct mass loss above 200 °C for **AQDS-Mg** and **AQDS-Cu**, attributed to the release of coordinated water (Figure S7–S9, Supporting Information). Regarding thermal stability, **AQDS-Na** and **AQDS-Mg** were stable up to 500 °C, while **AQDS-Cu** began to decompose at 400 °C, indicating that all **AQDS CPs** possess good thermal stability. Scanning electron microscopy (SEM) revealed that the **AQDS CP** crystals exhibit similar morphologies, while energy-dispersive X-ray spectroscopy (EDS) confirming the homogeneous distribution of the constituent elements in each material (Figure S10–S12, Supporting Information). Electrical conductivity measurements were performed on pressed pellets of **AQDS CPs** at 293 K under ambient conditions using a two-probe setup (Figure S13–S16, Supporting Information). The room-temperature conductivities of **AQDS-Na**, **AQDS-Mg,** and **AQDS-Cu** were measured to be 2.8×10^{-10}, $\approx 10^{-13}$, and $\approx 10^{-12}$ S cm^{-1}, respectively. Although all materials are highly insulating, **AQDS-Na** exhibited the highest conductivity among the series.

2.3. Quantum-Chemical Calculations

Theoretical calculations were performed under the density functional theory (DFT) to shed light on the electronic properties of the **AQDS CPs** (see the SI for computational details). **AQDS-Na** and **AQDS-Mg** crystal structures as extracted from the X-ray data were selected as representative examples of this material family, which features different crystal packing arrangements. The molecular electrostatic potential of the isolated AQDS ligand, calculated at the hybrid-DFT level (HSE06/6-31 G(d,p)),[47,48] reveals electron density accumulation around the oxygen atoms of both the AQ and sulfone groups (**Figure 2**a), suggesting stabilizing interactions with Li^+ Na^+ cations, relevant for LIBs and SIBs. In the periodic **AQDS CP** crystal structures, the Hartree potential calculated in periodic boundary conditions further indicates a strong tendency for the cation interaction with the AQ oxygen atoms (Figure S17, Supporting Information). In contrast, interactions with the sulfonate groups are sterically hindered and electrostatically less favorable, consistent with the expected electron-withdrawing behavior of these groups upon coordination with metal cations.

Electronic band structures calculated at the HSE06 level for the periodic crystals (reciprocal space of a triclinic Bravais lattice)

Research Article
doi.org/10.1002/batt.202500360
Chemistry Europe
European Chemical Societies Publishing

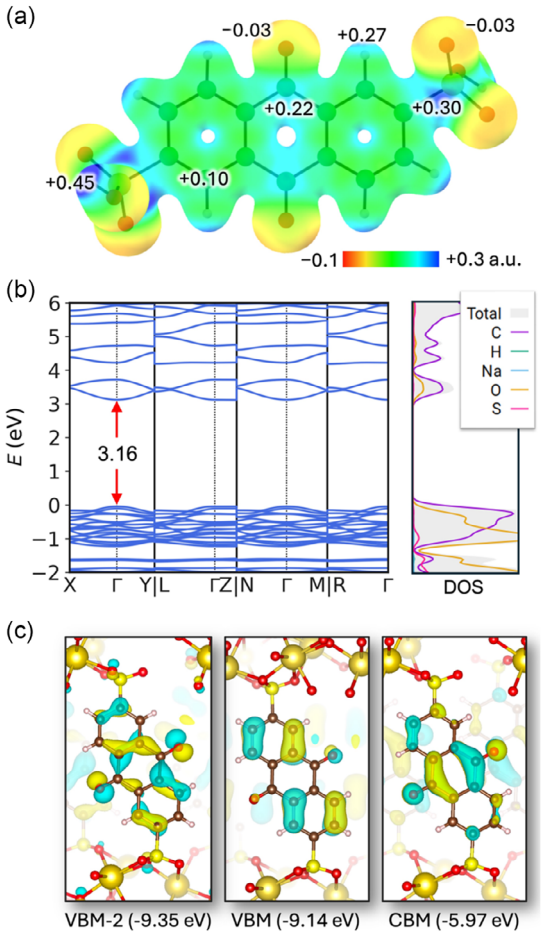

Figure 2. a) Molecular electrostatic potential of the minimum-energy structure of **AQDS**, computed at the HSE06/6-31 G(d,p) level and mapped onto the electron density surface (isovalue = 0.03 a.u.). b) Electronic band structure and species-projected density of states (DOS) for **AQDS-Na** calculated at the HSE06 level/tier-1 (light) numerical atom centered basis set. c) Selected frontier crystal orbitals (isovalue = 0.03 a.u.) of **AQDS-Na**. VBM and CBM denote the VB maximum and conduction band minimum, respectively.

indicate moderate dispersion of the energy levels near the bandgap (Figure 2b for **AQDS-Na** and Figure S18, Supporting Information for **AQDS-Mg**), particularly in the conduction band (CB), where the calculated effective masses for the electron transport (m_e) are close to the free electron mass (m_0). For **AQDS-Na**, m_e is predicted to be 0.6 m_0, whereas **AQDS-Mg** exhibits a higher value of 1.2 m_0. The bandgap is fully defined by the AQDS ligand, as evidenced by the dominant carbon and oxygen contributions in the species-projected density of states (Figure 2b). Whereas the topology of the CB minimum for both **AQDS-Na** (Figure 2c) and **AQDS-Mg** (Figure S19, Supporting Information) closely resembles the lowest-unoccupied molecular orbital of AQDS (Figure S20, Supporting Information), the valence band (VB) maximum is predicted to be of π nature for **AQDS-Na** and of n-type character (oxygen lone pairs) in **AQDS-Mg**. These two types of crystal orbitals lie within a narrow energy window ($\leq$0.2 eV), similar to the spacing observed for the corresponding molecular orbitals of AQDS. The calculated bandgap for **AQDS-Na** is 3.17 eV (Γ-centered), which is 0.34 eV smaller than that of **AQDS-Mg** (3.51 eV, centered at the N point). This difference may be attributed to the weaker polarization effect of Na^+ relative to Mg^{2+}, which leads to an upward shift of the VB maximum. In fact, we predict a larger charge accumulation on the AQ unit in the Na-based CP (−1.80 e) compared to its Mg-based analogue (−0.81 e). These results help explain the enhanced charge transport properties observed experimentally for the sodium derivative, although its wide bandgap still limits its performance as an intrinsic electronic conductor.

As the electronic properties of the materials are dictated by the AQDS organic system, electronic coupling ($|V|$) calculations were performed using the dimer projection (DIPRO)[49] approach at the semiempirical GFN2-xTB level[50] for the various ligand dimers present in **AQDS-Na** and **AQDS-Mg** (Figure S21, Supporting Information). The results predict small to negligible couplings ($|V| \leq 5$ meV) for hole transport in **AQDS CPs** (Table S2, Supporting Information), consistent with the relatively flat VB energy levels observed in their band structures ($m_h > 2\ m_0$, Figure 2b and Figure S18, Supporting Information). In contrast, theoretical calculations confirm strong electronic coupling for electron transport, with $|V|$ values as large as 53 meV for **AQDS-Na** and 35 meV for **AQDS-Mg** in the most strongly interacting dimers. Careful inspection of the **AQDS-Na** and **AQDS-Mg CP** structures (Figure S22, Supporting Information) reveals notable differences in the stacking of the **AQDS** dimers, including the lateral offset (3.91 vs. 4.82 Å), centroid-to-centroid distance (4.91 vs. 5.77 Å), and interplanar separation (3.13 vs 3.33 Å), supporting a more efficient electronic communication in the Na-based CP.

2.4. Electrochemical Performance of AQDS CPs

The electrochemical performance of the **AQDS CPs** was evaluated as cathode materials for Li-ion and Na-ion storage. The electrodes were fabricated using a mixture of **AQDS CPs** (active material), super P carbon (conductive additive), and polyvinylidene fluoride (PVDF binder) in a weight ratio of 50:40:10. It is important to note that a relatively high percentage of conductive additives (40%) was used to compensate for the insulating nature of these materials. Electrochemical experiments were carried out in coin-type half-cells, using Li or Na metal as both the pseudo-reference and counter electrodes (see SI for experimental details). For Li-ion storage testing, the electrolyte consisted of 1 M lithium bis(trifluoromethanesulfonyl)imide (LiTFSI) dissolved in a (1:1, v/v) mixture of dioxolane (DOL) and dimethoxyethane (DME). For Na-ion storage, 1 M sodium hexafluorophosphate ($NaPF_6$) in DME was used to enable direct comparison with previous studies.[42] The electrodes were prepared with a target mass loading of 2–3 mg cm^{-2} of active material (**AQDS CPs**).

We first evaluated the cycling stability of **AQDS CPs** as cathodes for Li-ion storage at a current density of 50 mA g^{-1} (**Figure 3**a). The theoretical specific capacities of **AQDS-Na**, **AQDS-Mg**, and **AQDS-Cu** are 130, 126, and 115 mAh g^{-1}, respectively. The initial discharge capacities were 120 mAh g^{-1} for **AQDS-Na**, 95 mAh g^{-1} for **AQDS-Mg**, and 106 mAh g^{-1} for **AQDS-Cu**. After 100 cycles, the capacity retention values were 51%, 52%, and 72%, respectively. Differential capacity (dQ/dV)

Research Article
doi.org/10.1002/batt.202500360
Chemistry Europe
European Chemical Societies Publishing

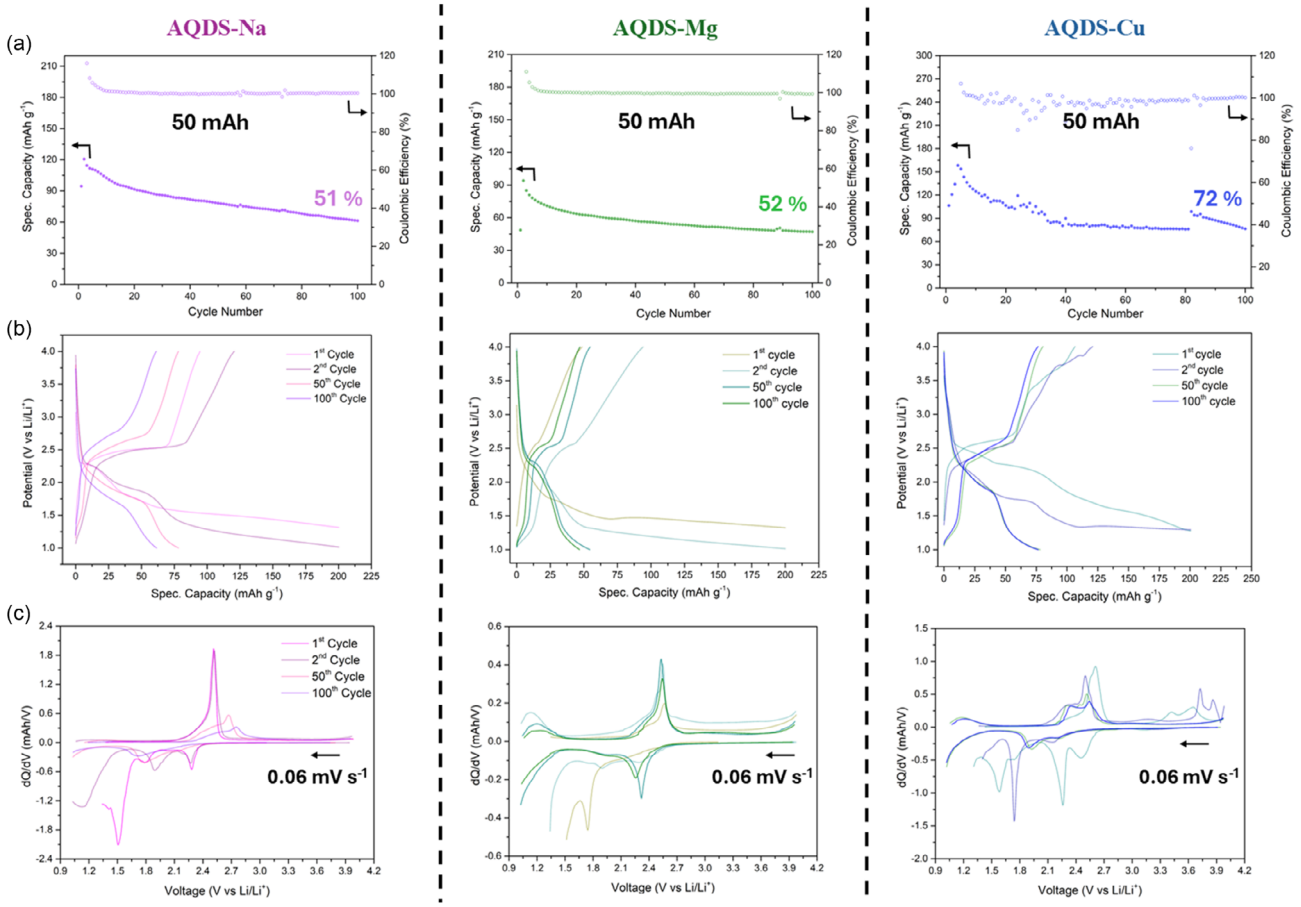

Figure 3. Galvanostatic charge–discharge cycling experiments of **AQDS CPs** in Li-based batteries with specific capacities of 61, 47, and 76 mAh g^{-1} for **AQDS-Na**, **AQDS-Mg,** and **AQDS-Cu**, respectively, after 100 cycles. a) Cycling stability and Coulombic efficiency at a current density of 50 mA g^{-1} within a potential window of 1.0–4.0 V versus Li/Li^+. b) Galvanostatic charge–discharge profiles recorded at the 1st, 2nd, 50th, and 100th cycles at 50 mA g^{-1}. c) Differential capacity (dQ/dV) plots corresponding to the 1st, 2nd, 50th, and 100th cycles, obtained at a scan rate of 0.06 mV s^{-1} over the voltage range of 1.0–4.0 V versus Li/Li^+.

analysis (Figure 3c) revealed a main redox signal associated with the two-electron reduction of the AQ moieties, centered at 2.39 V and 2.43 V versus Li/Li^+ for **AQDS-Na** and **AQDS-Mg**, respectively, both of which gradually decreased in intensity upon cycling. In the case of **AQDS-Cu**, two distinct redox peaks were observed at 2.12 and 2.39 V versus Li/Li^+, corresponding to two sequential one-electron redox processes.

The three **AQDS CPs** were subsequently evaluated as cathode materials for Na-ion storage to assess the impact of the Na^+ ion size on electrochemical performance. In this case, more pronounced differences were observed in the practical capacities among the materials (**Figure 4**). After 100 cycles, the specific capacities were 91, 47, and 18 mAh g^{-1} for **AQDS-Na**, **AQDS-Mg,** and **AQDS-Cu**, respectively. Therefore, while **AQDS-Na** exhibits improved electrochemical performance when used as a cathode in SIBs, compared with LIBs, both **AQDS-Mg** and **AQDS-Cu** show significant reductions in specific capacity and capacity retention when replacing Li^+ with Na^+. The average sodium storage voltage follows the trend from AQDS-Na < AQDS-Mg < AQDS-Cu (1.79 V < 1.84 V < 1.90 V vs. Na^+/Na). In addition, when the current density was decreased to 10 mA g^{-1}, the specific capacity of **AQDS-Mg** increased to 74 mAh g^{-1} (Figure S23, Supporting Information). To confirm whether these differences in electrochemical performance are due to diffusion effects, galvanostatic intermittent titration technique (GITT) measurements were conducted to unveil the kinetic behavior of the three **AQDS CPs** (Figure S24, Supporting Information). GITT was conducted in a two-electrode configuration with Na metal as the counter and reference electrodes. The diffusion coefficients of Na^+ are approximatively the same order of magnitude for all three **AQDS CPs** ($\approx 10^{-12}$ cm^2 s^{-1}). Therefore, given that the diffusion coefficients and interplanar distances between AQ moieties are comparable across all three **AQDS CPs**, the key structural difference influencing performance appears to be the presence of coordinated water molecules and vacancy defects. It has been reported that coordinated water in cathode materials can significantly affect the performance and safety of SIBs,[51,52] primarily due to its ability to form hydrogen bonds with interstitial water and to combine with Na^+ to form $[Na(OH_2)]^+$ in the electrolyte, leading to side reactions and safety concerns.[52] Thus, the presence of coordinated water in **AQDS-Mg** and **AQDS-Cu** has a critical impact on their performance when evaluated as cathodes for Na-ion storage.

The different electrochemical performances of **AQDS CPs** in Li and Na batteries are more evident in the rate capability tests

Research Article
doi.org/10.1002/batt.202500360
Chemistry Europe
European Chemical Societies Publishing

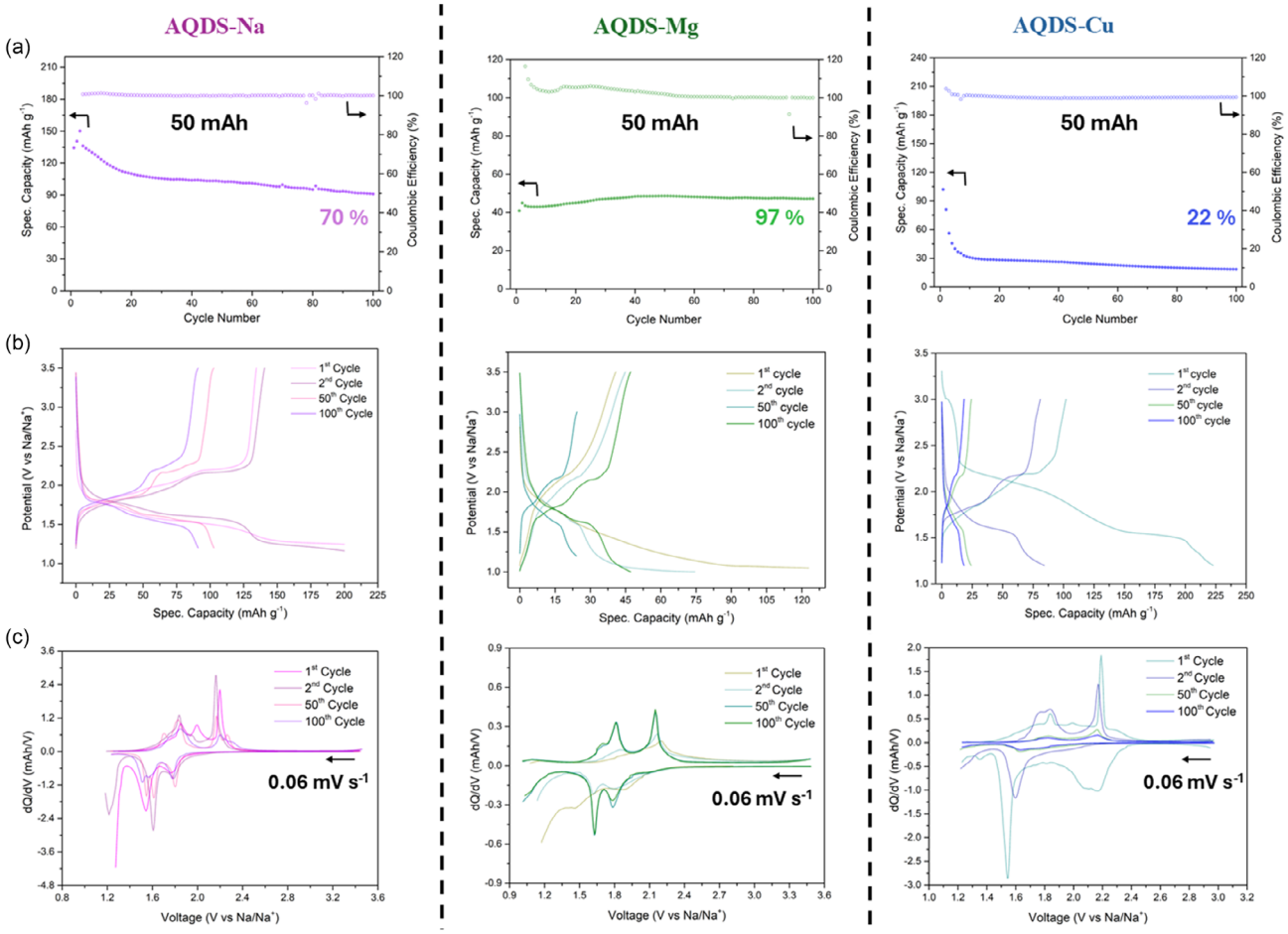

Figure 4. Galvanostatic charge–discharge cycling experiments of **AQDS CPs** in Na-based batteries with specific capacities of 91, 47, and 18 mAh g^{-1} for **AQDS-Na**, **AQDS-Mg,** and **AQDS-Cu**, respectively, after 100 cycles. a) Cycling stability and Coulombic efficiency of **AQDS-CPs** at a current density of 50 mA g^{-1} within a potential window of 1.2–3.5 V versus Na/Na^+. b) Galvanostatic charge–discharge profiles of the 1st, 2nd, 50th, and 100th cycles at 50 mA g^{-1}. c) Differential capacity (dQ/dV) plots of the 1st, 2nd, 50th, and 100th cycles, measured at a scan rate 0.06 mV s^{-1} over a voltage range of 1.0–3.6 V versus Na/Na^+.

(**Figure 5**). Overall, **AQDS-Na** shows a better rate performance in both Li and Na batteries when compared to the other two CPs. At low C-rates (C/10 to C/2), **AQDS-Na** shows practical capacities close to the theoretical values (130 mAh g^{-1}). **AQDS-Cu** and **AQDS-Mg** showed the lowest rate performance when used as cathodes in Na batteries. In contrast, **AQDS-Cu** significantly

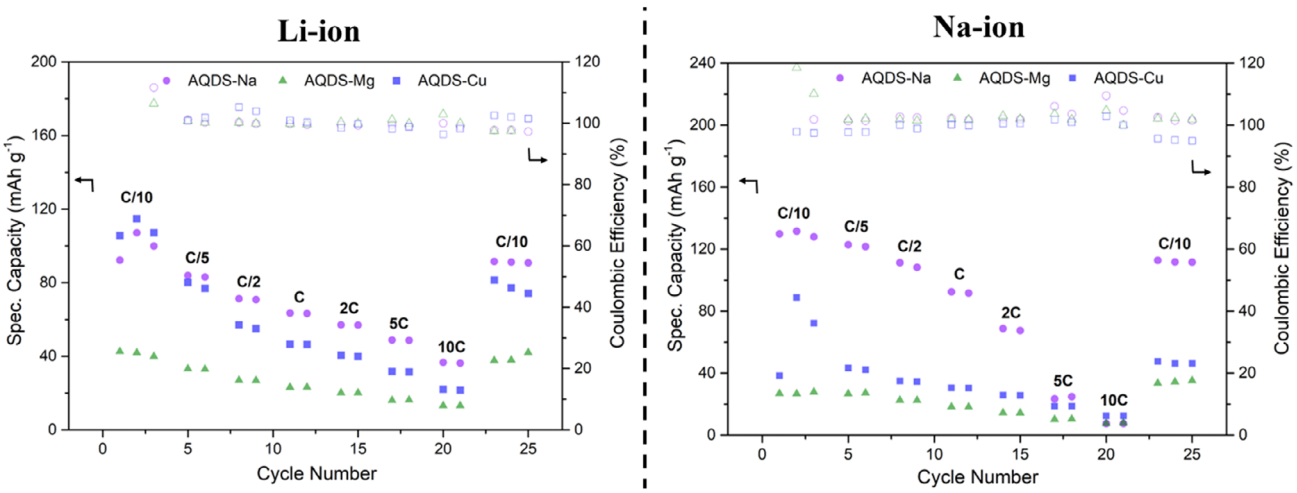

Figure 5. Rate capability performance of **AQDS CPs** as a function of cycle number using a potential window of 1.4–3.8 V, with current rates (C-rates) from C/10 up to 10C.

improves its performance for Li-ion storage, which is also reflected in its cycling stability. **AQDS-Cu** achieves a higher capacity of 115 mAh g^{-1} at C/10, decreasing with increasing C-rate. **AQDS-Mg** performs better as a cathode for Li-ion storage; however, compared to the other two CPs, it exhibits the lowest rate performance overall.

3. Conclusion

In summary, we have synthesized and structurally characterized a series of anthraquinone-disulfonate CPs (**AQDS-Na**, **AQDS-Mg**, and **AQDS-Cu**) and evaluated their potential as cathode materials for Li-ion and Na-ion storage. Despite their similar chemical composition and theoretical capacities, the **AQDS CPs** exhibit markedly different electrochemical performances, which are strongly linked to their structural features. **AQDS-Na**, featuring a 3D framework without coordinated water molecules, displays superior capacity retention and stability, particularly for Na-ion storage (capacity of 91 mAh g^{-1} after 100 cycles). In contrast, the 2D structures of **AQDS-Mg** and **AQDS-Cu**, containing coordinated water, exhibit lower practical capacities, especially upon cycling with Na^+ ions (capacities of 47 and 18 mAh g^{-1} after 100 cycles for **AQDS-Mg** and **AQDS-Cu**, respectively). Our results highlight the critical role of framework dimensionality, hydration state, and metal–linker interactions in tuning ion/electron transport properties and long-term cycling stability of organic-based cathode materials. In particular, we emphasize the negative impact of coordinated water on the electrochemical performance of **AQDS-Mg** and **AQDS-Cu**. Complementary quantum-chemical calculations confirm that electronic transport is primarily governed by **AQDS**-derived molecular orbitals, with stronger electron coupling and lower CB energy in **AQDS-Na** contributing to its enhanced performance, despite the materials' inherently large bandgaps. This work provides valuable design principles for the development of future redox-active CPs and framework materials for sustainable and efficient energy storage systems based on earth-abundant elements.

Acknowledgements

This work has received funding from the European Research Council (ERC) under the European Union's Horizon Europe Framework Programme (ERC-2021-Starting Grant, grant agreement no. 101039748-ELECTROCOFS), from the FCT/MEC (CICECO-Aveiro Institute of Materials, UIDB/50011/2020, UIDP/50011/2020, LA/P/0006/2020), FCT (PTDC/QUI-ELT/2593/2021), from the Spanish Government (COFCAT, PID2023-152083OA-I00, PID2020-119748GA-I00 and TED2021-131255B-C44), and from the PRR—Plano de Recuperação e Resiliência (NextGenerationEU funds) through the scope of the Agenda for Business Innovation "New Generation Storage" (project no. 58 with the application C644936001–00000045). This work has also received financial support from the Xunta de Galicia (Centro singular de investigación de Galicia accreditation 2023–2027, ED431G 2023/03) and the Oportunius program (Gain). A.F.-A. acknowledges Generalitat Valenciana for a postdoctoral contract (CIAPOS/2023/316). R.M. and A.V. acknowledge financial support from F.R.S.-FNRS through ASP PhD fellowship and Excellence of Science (EOS) program—ECOBAT [40007515], respectively.

Conflict of Interest

The authors declare no conflict of interest.

Data Availability Statement

The data that support the findings of this study are available from the corresponding author upon reasonable request.

Keywords: anthraquinones · cathode materials · coordination polymers · lithium-ion batteries · organic electrode materials · sodium-ion batteries

[1] B. Dunn, H. Kamath, J.-M. Tarascon, *Science* **2011**, *334*, 928.
[2] R. Usiskin, Y. Lu, J. Popovic, M. Law, P. Balaya, Y.-S. Hu, J. Maier, *Nat. Rev. Mater.* **2021**, *6*, 1020.
[3] S. Bobba, S. Carrara, J. Huisman, F. Mathieux, C. Pavel, *Eur. Comm.* **2020**.
[4] Y. Lu, Q. Zhang, L. Li, Z. Niu, J. Chen, *Chem* **2018**, *4*, 2786.
[5] Y. Lu, J. Chen, *Nat. Rev. Chem.* **2020**, *4*, 127.
[6] P. Poizot, J. Gaubicher, S. Renault, L. Dubois, Y. Liang, Y. Yao, *Chem. Rev.* **2020**, *120*, 6490.
[7] B. Esser, F. Dolhem, M. Becuwe, P. Poizot, A. Vlad, D. Brandell, *J. Power Sources* **2021**, *482*, 228814.
[8] J. Bitenc, K. Pirnat, O. Lužanin, R. Dominko, *Chem. Mater.* **2024**, *36*, 1025.
[9] R. Wessling, P. Penert, B. Esser, *Adv. Energy Mater.* **2025**, *15*, 2500150.
[10] P. Gerlach, A. Balducci, *ChemElectroChem* **2020**, *7*, 2364.
[11] M. Armand, S. Grugeon, H. Vezin, S. Laruelle, P. Ribière, P. Poizot, J.-M. Tarascon, *Nat. Mater.* **2009**, *8*, 120.
[12] K. Lei, F. Li, C. Mu, J. Wang, Q. Zhao, C. Chen, J. Chen, *Energy Environ. Sci.* **2017**, *10*, 552.
[13] T. Chen, H. Banda, J. Wang, J. J. Oppenheim, A. Franceschi, M. Dincă, *ACS Cent. Sci.* **2024**, *10*, 569.
[14] A. N. Davis, K. Parui, M. M. Butala, A. M. Evans, *Nanoscale* **2024**, *16*, 10142.
[15] S. Muench, A. Wild, C. Friebe, B. Häupler, T. Janoschka, U. S. Schubert, *Chem. Rev.* **2016**, *116*, 9438.
[16] T. B. Schon, B. T. McAllister, P. F. Li, D. S. Seferos, *Chem. Soc. Rev.* **2016**, *45*, 6345.
[17] T. Janoschka, M. D. Hager, U. S. Schubert, *Adv. Mater.* **2012**, *24*, 6397.
[18] R. Dantas, C. Ribeiro, M. Souto, *Chem. Commun.* **2024**, *60*, 138.
[19] S. Haldar, A. Schneemann, S. Kaskel, *J. Am. Chem. Soc.* **2023**, *145*, 13494.
[20] G. Valente, R. Dantas, P. Ferreira, R. Grieco, N. Patil, A. Guillem-Navajas, D. Rodríguez-San Miguel, F. Zamora, R. Guntermann, T. Bein, J. Rocha, M. H. Braga, K. Strutyński, M. Melle-Franco, R. Marcilla, M. Souto, *J. Mater. Chem. A* **2024**, *12*, 24156.
[21] Z. Zhang, K. Awaga, *MRS Bull* **2016**, *41*, 883.
[22] R. Zhao, Z. Liang, R. Zou, Q. Xu, *Joule* **2018**, *2*, 2235.
[23] M. Souto, K. Strutyński, M. Melle-Franco, J. Rocha, *Chem. Eur. J.* **2020**, *26*, 10912.
[24] K. Zhang, C. Guo, Q. Zhao, Z. Niu, J. Chen, *Adv. Sci.* **2015**, *2*, 1500018.
[25] Z. Song, Y. Qian, M. L. Gordin, D. Tang, T. Xu, M. Otani, H. Zhan, H. Zhou, D. Wang, *Angew. Chem. Int. Ed.* **2015**, *54*, 13947.
[26] J. Bitenc, K. Pirnat, T. Banăiă, M. Gaberšăek, B. Genorio, A. Randon-Vitanova, R. Dominko, *ChemSusChem* **2015**, *8*, 4128.
[27] B. Pan, J. Huang, Z. Feng, L. Zeng, M. He, L. Zhang, J. T. Vaughey, M. J. Bedzyk, P. Fenter, Z. Zhang, A. K. Burrell, C. Liao, *Adv. Energy Mater.* **2016**, *6*, 1600140.
[28] C. R. Deblase, K. E. Silberstein, T. T. Truong, H. D. Abruña, W. R. Dichtel, *J. Am. Chem. Soc.* **2013**, *135*, 16821.
[29] S. Wang, Q. Wang, P. Shao, Y. Han, X. Gao, L. Ma, S. Yuan, X. Ma, J. Zhou, X. Feng, B. Wang, *J. Am. Chem. Soc.* **2017**, *139*, 4258.

[30] O. Lužanin, R. Dantas, R. Dominko, J. Bitenc, M. Souto, *J. Mater. Chem. A* **2023**, *11*, 21553.
[31] J. Liu, K. Guo, W. Guo, J. Chang, Y. Li, F. Bao, *Angew. Chem. Int. Ed.* **2025**, *64*, e202424494.
[32] Z. Zhang, H. Yoshikawa, K. Awaga, *J. Am. Chem. Soc.* **2014**, *136*, 16112.
[33] Z. Zhang, H. Yoshikawa, K. Awaga, *Chem. Mater.* **2016**, *28*, 1298.
[34] J. Liu, Y. Zhou, G. Xing, M. Qi, Z. Tang, O. Terasaki, L. Chen, *Adv. Funct. Mater.* **2024**, *34*, 2312636.
[35] C. Ribeiro, B. Tan, F. Figueira, R. F. Mendes, J. Calbo, G. Valente, P. Escamilla, F. A. A. Paz, J. Rocha, M. Dincă, M. Souto, *J. Am. Chem. Soc.* **2025**, *147*, 63.
[36] Y. Zhang, J. Wang, P. Apostol, D. Rambabu, A. Eddine Lakraychi, X. Guo, X. Zhang, X. Lin, S. Pal, V. Rao Bakuru, X. Chen, A. Vlad, *Angew. Chem. Int. Ed.* **2023**, *62*, e202310033.
[37] S.-S. Bao, G. K. H. Shimizu, L.-M. Zheng, *Coord. Chem. Rev.* **2019**, *378*, 577.
[38] G. Zhang, H. Fei, *Chem. Commun.* **2017**, *53*, 4156.
[39] D. K. Panda, K. Maity, A. Palukoshka, F. Ibrahim, S. Saha, *ACS Sustain. Chem. Eng.* **2019**, *7*, 4619.
[40] Y.-S. Tsai, S.-C. Yang, T.-H. Yang, C.-H. Wu, T.-C. Lin, C.-W. Kung, *ACS Appl. Mater. Interfaces* **2024**, *16*, 62185.
[41] W. Wan, H. Lee, X. Yu, C. Wang, K.-W. Nam, X.-Q. Yang, H. Zhou, *RSC Adv.* **2014**, *4*, 19878.
[42] W. Tang, R. Liang, D. Li, Q. Yu, J. Hu, B. Cao, C. Fan, *ChemSusChem* **2019**, *12*, 2181.
[43] F. Gándara, E. G. Puebla, M. Iglesias, D. M. Proserpio, N. Snejko, M. Á. Monge, *Chem. Mater.* **2009**, *21*, 655.
[44] A. E. Platero-Prats, M. Iglesias, N. Snejko, Á. Monge, E. Gutiérrez-Puebla, *Cryst. Growth Des.* **2011**, *11*, 1750.
[45] C. Shi, M. Gomez-Mendoza, E. Gómez de Oliveira, M. García-Tecedor, M. Barawi, F. Esteban-Betegón, M. Liras, E. Gutiérrez-Puebla, A. Monge, V. A. de la Peña O'Shea, F. Gándara, *Chem. Sci.* **2024**, *15*, 6860.
[46] Deposition numbers 2446663 (for **AQDS-Na**), and 2446662 (for **AQDS-Cu**) contain the supplementary crystallographic data for this paper. These data are provided free of charge by the joint Cambridge Crystallographic Data Centre and Fachinformationszentrum Karlsruhe Access Structures service.
[47] A. V. Krukau, O. A. Vydrov, A. F. Izmaylov, G. E. Scuseria, *J. Chem. Phys.* **2006**, *125*, 224106.
[48] R. Ditchfield, W. J. Hehre, J. A. Pople, *J. Chem. Phys.* **1971**, *54*, 724.
[49] B. Braumeier, J. Kirkpatrick, D. Andrienko, *Phys. Chem. Chem. Phys.* **2010**, *12*, 11103.
[50] C. Bannwarth, S. Ehlert, S. Grimme, *J. Chem. Theory Comput.* **2019**, *15*, 1652.
[51] Y. You, X.-L. Wu, Y.-X. Yin, Y.-G. Guo, *Energy Environ. Sci.* **2014**, *7*, 1643.
[52] X. Xu, S. Zhu, C. Yang, Y. Wang, Z. Wu, J. Zheng, Y. Wub, Y. Gao, *J. Mater. Chem. A* **2025**, *13*, 11848.

Manuscript received: May 11, 2025
Revised manuscript received: June 13, 2025
Version of record online: